

## Low-lying dipole strength distribution in $^{204}\text{Pb}$

T. Shizuma,<sup>1</sup> S. Endo,<sup>2</sup> A. Kimura,<sup>2</sup> R. Massarczyk,<sup>3</sup> R. Schwengner<sup>ⓧ</sup>,<sup>4</sup> R. Beyer,<sup>4</sup> T. Hensel<sup>ⓧ</sup>,<sup>4</sup> H. Hoffmann,<sup>4</sup> A. Junghans<sup>ⓧ</sup>,<sup>4</sup> K. Römer,<sup>4</sup> S. Turkat,<sup>5</sup> A. Wagner<sup>ⓧ</sup>,<sup>4</sup> and N. Tsoneva<sup>ⓧ</sup><sup>6</sup>

<sup>1</sup>*National Institutes for Quantum Science and Technology, Tokai, Ibaraki 319-1106, Japan*

<sup>2</sup>*Japan Atomic Energy Agency, Tokai, Ibaraki 319-1195, Japan*

<sup>3</sup>*Los Alamos National Laboratory, Los Alamos, New Mexico 87545, USA*

<sup>4</sup>*Helmholtz-Zentrum Dresden-Rossendorf, 01328 Dresden, Germany*

<sup>5</sup>*Institut für Kern- und Teilchenphysik, Technische Universität Dresden, 01069 Dresden, Germany*

<sup>6</sup>*Extreme Light Infrastructure (ELI-NP), Horia Hulubei National Institute for R&D in Physics and Nuclear Engineering (IFIN-HH), 077125 Bucharest-Magurele, Romania*

 (Received 1 June 2022; revised 8 August 2022; accepted 13 October 2022; published 26 October 2022)

Dipole and quadrupole strength distribution of  $^{204}\text{Pb}$  was investigated via a nuclear resonance fluorescence experiment using bremsstrahlung produced using an electron beam at a kinetic energy of 10.5 MeV at the linear accelerator ELBE. We identified 136 states resonantly excited at energies from 3.6 to 8.4 MeV. Spins of the excited states were deduced by angular distribution ratios of  $\gamma$  rays observed at scattering angles of  $90^\circ$  and  $127^\circ$  with respect to the incident  $\gamma$  beam. The analysis of the measured  $\gamma$ -ray spectra includes the quasicontinuum of levels at high energy. Monte Carlo simulation of  $\gamma$ -ray cascades were performed to obtain the intensities of inelastic transitions and branching ratios of the ground-state transitions. The present experimental results were used to investigate the electric dipole ( $E1$ ) strengths by comparison with predictions from the quasiparticle-phonon model with the self-consistent energy density functional.

DOI: [10.1103/PhysRevC.106.044326](https://doi.org/10.1103/PhysRevC.106.044326)

### I. INTRODUCTION

Low-lying electric dipole ( $E1$ ) excitation in atomic nuclei has attracted considerable interest during the past decades, caused by significant progress in experimental and theoretical studies of its properties [1,2]. It has been observed as a local accumulation of the  $E1$  strength at the low-energy tail of the giant dipole resonance (GDR) in both stable and unstable nuclei over a broad range of nuclei [3–12]. This structure is commonly denoted as the pygmy dipole resonance (PDR), because the  $E1$  strength is weak relative to that of the GDR, which exhausts almost all the  $E1$  strength predicted by the Thomas-Reiche-Kuhn (TRK) sum rule [13].

The geometric picture of the PDR is an out-of-phase oscillation of excess neutrons against an almost isospin-saturated ( $N \approx Z$ ) core [14–16]. Microscopically, the PDR is explained as a sequence of excited one-particle-one-hole excitations (1p-1h), which act coherently and therefore cause an increased transition strength [17,18]. Since the PDR strength is correlated with the neutron skin thickness [19,20] which is related to nuclear symmetry energy [21,22] and the equation of state of the neutron-rich matter [23], the investigation of the PDR may provide useful information on the properties of the neutron stars [24].

Another interesting aspect of low-energy excitations, and in particular of the PDR, is that they involve interactions resulting from binding of complex configurations and the GDR related to nuclear polarization effects. A quasiparticle-random-phase-approximation (QRPA), taking into account

only coherence superpositions of two-quasiparticle excitations is not enough to explain in detail the structure of nuclear excited states in the PDR region. Rather, an expanded approach is needed which explicitly takes into account the interactions between multi-quasi-particle configurations.

Furthermore, recent studies of nuclear reactions of astrophysical interest show that the reaction cross sections strongly depend on the low-energy part of the electromagnetic dipole strength function and the PDR [12,25,26]. Such enhancement can have a strong impact on nucleosynthesis of heavier elements in stellar environments [12,26]. It is known that lead isotopes may play important role in the s-process of nucleosynthesis. From our previous studies in the semimagic  $^{206}\text{Pb}$  nucleus we found that the presence of a PDR mode can affect the  $^{205}\text{Pb}$  radiative neutron capture cross section, a reaction of relevance to the destruction of  $^{205}\text{Pb}$  during the s-process [12].

The stable lead isotopes including  $^{204}\text{Pb}$  are suitable for studying the PDR since they exhibit an appreciable amount of low-lying dipole strength [4,12,27]. So far, the low-lying dipole distribution below 6.75 MeV in  $^{204}\text{Pb}$  has been measured in nuclear resonance fluorescence (NRF) experiments with bremsstrahlung [27]. In the present work, the information was extended up to the neutron separation energy of 8.395 MeV by using higher-energy bremsstrahlung. The experimental results are compared with predictions from the self-consistent energy density-functional (EDF) theory and the three-phonon quasiparticle-phonon model (QPM) [15,17,18].

## II. EXPERIMENTAL PROCEDURE

The present NRF measurement on  $^{204}\text{Pb}$  was carried out at the bremsstrahlung facility  $\gamma\text{ELBE}$  [28] of the Helmholtz-Zentrum Dresden-Rossendorf. Bremsstrahlung was produced using an electron beam at a kinetic energy of 10.5 MeV with an average beam current of  $620\ \mu\text{A}$  at a micropulse repetition rate of 13 MHz. The electron beam hit a radiator consisting of a niobium foil with a thickness of  $7\ \mu\text{m}$ . The electron energy was chosen as the flux was sufficiently high up to the neutron separation energy. The bremsstrahlung was collimated by an Al collimator with a length of 2.6 m and an opening angle of 5 mrad. A cylindrical Al absorber with a length of 10 cm was placed between the radiator and the collimator to reduce the low-energy bremsstrahlung.

The target consisted of a metallic disk of  $^{204}\text{Pb}$  with a diameter of 20 mm tilted by  $45^\circ$  about a vertical axis perpendicular to the beam. The target mass was 1.9 g, enriched to 99.94% in  $^{204}\text{Pb}$ . The lead disk was combined with 300 mg of boron, enriched to 99.5% in  $^{11}\text{B}$ , that was also shaped to a disk of 20 mm diameter to determine the photon flux from known scattering cross sections of levels in  $^{11}\text{B}$ .

Scattered photons were measured with four high-purity germanium (HPGe) detectors with relative efficiencies of 100%. All HPGe detectors were surrounded by escape-suppression shields made of bismuth germanate (BGO) scintillation detectors. Two HPGe detectors were placed horizontally at  $90^\circ$  relative to the photon beam direction at a distance of 28 cm from the target. The other two HPGe detectors were placed vertically at  $127^\circ$  to the beam at a distance of 32 cm from the target. The ratios of the  $\gamma$ -ray intensities measured at  $90^\circ$  and  $127^\circ$  are used to distinguish between dipole and quadrupole radiation. To reduce the contribution of low-energy photons, absorbers of 8-mm Pb plus 3-mm Cu were placed in front of the detectors at  $90^\circ$ , and 3-mm Pb plus 3-mm Cu were used for the detectors at  $127^\circ$ . Spectra of scattered photons were measured for 132 h. Part of a spectrum including events measured with the two detectors at  $127^\circ$  relative to the beam is shown in Fig. 1. Further details of the measurement techniques are given in Refs. [29,30].

## III. RESULTS

### A. Integrated scattering cross sections

In photon scattering experiments, the energy-integrated scattering cross section  $I_s$  of an excited state at the energy of  $E_x$  can be deduced from the measured intensity of the respective transitions to the ground state (g.s.) [31]. It can be determined relative to the known integrated scattering cross sections  $I_s(E_x^B)$  of states in  $^{11}\text{B}$  [32]:

$$\frac{I_s(E_x)}{I_s(E_x^B)} = \left[ \frac{I_\gamma(E_\gamma, \theta)}{W(E_\gamma, \theta)\Phi_\gamma(E_x)N_N\lambda} \right] \times \left[ \frac{I_\gamma(E_\gamma^B, \theta)}{W(E_\gamma^B, \theta)\Phi_\gamma(E_x^B)N_N^B\lambda^B} \right]^{-1}. \quad (1)$$

Here  $I_\gamma(E_\gamma, \theta)$  and  $I_\gamma(E_\gamma^B, \theta)$  denote efficiency-corrected intensities of a ground-state transition at  $E_\gamma$  and of a ground-state transition in  $^{11}\text{B}$  at  $E_\gamma^B$ , respectively, observed at a

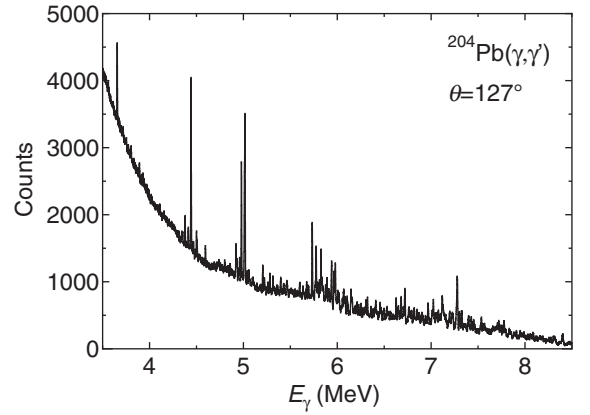


FIG. 1. Part of a spectrum of photons scattered from  $^{204}\text{Pb}$  combined with  $^{11}\text{B}$ , measured during the irradiation with bremsstrahlung produced by electrons at the kinetic energy of 10.5 MeV. This spectrum is the sum of the spectra measured with the two detectors at  $127^\circ$  relative to the beam.

scattering angle  $\theta$  to the beam.  $W(E_\gamma, \theta)$  and  $W(E_\gamma^B, \theta)$  represent the angular correlations of  $\gamma$  rays in these transitions. The quantities  $\Phi_\gamma(E_x)$  and  $\Phi_\gamma(E_x^B)$  are the photon fluxes at the energy of the considered level and at the energy of a level in  $^{11}\text{B}$ , respectively. The quantities  $N_N$  and  $N_N^B$  stand for the numbers of nuclei in the  $^{204}\text{Pb}$  and  $^{11}\text{B}$  targets, respectively. The quantities  $\lambda$  and  $\lambda^B$  are the correction factors of atomic and self-absorption for the levels at  $E_x$  in  $^{204}\text{Pb}$  and at  $E_x^B$  in  $^{11}\text{B}$ , respectively. These correction factors were determined according to Eq. (19) in Ref. [33]. The determination of the integrated cross sections relative to the ones of states in  $^{11}\text{B}$  has the advantage that the efficiencies of the detectors and the photon flux are needed in relative units only. We calculated the energy-dependent efficiencies for the four HPGe detectors by using GEANT4 [34]. The simulated efficiency curves were checked by using efficiencies measured with a  $^{226}\text{Ra}$  calibration source. The photon-flux spectrum was calculated using a bremsstrahlung computer code [35] based on the Born approximation with Coulomb correction [36] and including an atomic screening correction [37]. The calculated curve of the photon flux fits the experimental value derived from measured intensities, known integrated cross sections [32] and angular distributions [38] of transitions in  $^{11}\text{B}$ .

The integrated scattering cross section  $I_s$  is related to the partial decay width  $\Gamma_0$  to the ground state and the total decay width  $\Gamma$  according to

$$I_s = \int \sigma_{\gamma\gamma} dE = \frac{2J_x + 1}{2J_0 + 1} \left( \frac{\pi \hbar c}{E_x} \right)^2 \frac{\Gamma_0^2}{\Gamma}, \quad (2)$$

where  $\sigma_{\gamma\gamma}$  is the elastic-scattering cross section,  $J_0$  and  $J_x$  denote the spins of the ground state and the excited state, respectively.

Spins of the excited states were deduced by comparing the ratios of  $\gamma$ -ray intensities measured with the HPGe detectors at two different angles with theoretical predictions. The optimum combination is angles of  $90^\circ$  and  $127^\circ$  because the ratios for the respective spin sequences 0–1–0 and 0–2–0 differ most at these angles.

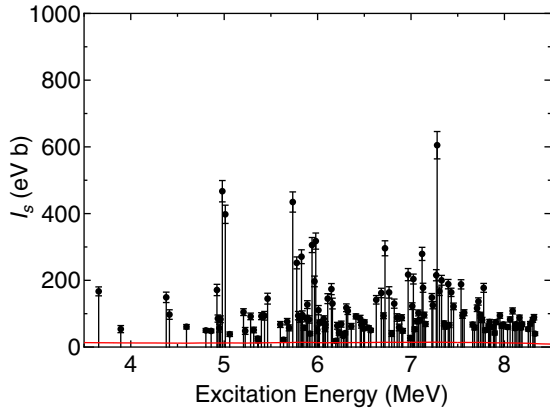


FIG. 2. Integrated scattering cross sections deduced from the present experiment. The detection limits for  $I_s$  are shown with a red line.

The expected values are  $W(90^\circ)/W(127^\circ)_{0-1-0} = 0.74$  and  $W(90^\circ)/W(127^\circ)_{0-2-0} = 2.18$ , taking into account the finite solid angle of the detectors.

The deduced values for excitation energies, angular distribution ratios, spin assignments, the ratios  $\Gamma_0^2/\Gamma$ , and branching ratios into the ground state are listed in Table I. Figure 2 shows the integrated cross sections deduced from the present experimental data. We observed 134 states with  $J = 1$  and 2 states with  $J = 2$  below the neutron separation energy, including 95 states newly identified in this work. A comparison of the  $\Gamma_0^2/\Gamma$  ratios obtained in the present experiment with previous work [27] is also shown in Table I. The present results are generally in good agreement with those previously published. Spins of 14 states known in previous work were newly determined. The present  $J = 1$  spin assignment for the 3893-keV level is not consistent with the previous  $J = 2$  assignment [27]. In addition, the resonance states at 5610 and 6420 keV reported previously [27] could not be confirmed. Compared to the previous measurement [27], the present  $\Gamma_0^2/\Gamma$  values are systematically larger for excitation energies up to about 5.5 MeV. Considering the higher bremsstrahlung endpoint energy used in the present measurement, this is most likely the results of feeding. Similar effects of the feeding are observed in  $^{90}\text{Zr}$  where levels in the range of  $E_x \approx 4$  to 6 MeV are mainly fed by levels above  $E_x \approx 6$  MeV [8].

The detection limit for a 95% confidence level is defined as  $A_{DL} = 2.8\sqrt{2B}$  [39], where  $B$  is the integral over a background interval of full width at half maximum of a nearby peak, which has been applied in similar experiments [40,41]. The detection limits converted to  $I_s$  is shown with a red line in Fig. 2. The state with the smallest  $I_s$  is the one at 6194 keV with 19(6) eV b. At this peak, we obtain  $A_{PEAK}/A_{DL} = 1.4(4)$  from the  $127^\circ$  spectra. Toward high energy, the background decreases rapidly, while the background integral increases. For the highest peak given in Fig. 2 at 8327 keV, we obtain  $A_{PEAK}/A_{DL} = 3.8(5)$ .

The reduced electric dipole transition probabilities  $B(E1) \uparrow$  can be extracted from  $\Gamma_0$  using the following relationship:

$$B(E1) \uparrow = 2.865 \frac{\Gamma_0}{E_\gamma^3} \times 10^{-3} \text{ e}^2 \text{ fm}^2, \quad (3)$$

TABLE I. Results of the  $^{204}\text{Pb}(\gamma, \gamma')$  measurements. The excitation energies  $E_x$ , the angular distribution ratios  $W(90^\circ)/W(127^\circ)$ , the spin assignments  $J$ , the ratios  $\Gamma_0^2/\Gamma$ , and the branching ratios  $\Gamma_0/\Gamma$  are given. The values of  $\Gamma_0^2/\Gamma$  known from previous measurements are also listed for comparison.

$E_x^a$ (keV)	$W(90^\circ)/$ $W(127^\circ)$	$J$	$\Gamma_0^2/\Gamma^b$ (eV)	$\Gamma_0/\Gamma$	$\Gamma_0^2/\Gamma^c$ (eV)
3656.5(1)	0.80(11)	1	0.194(16)	1.0	0.12(1)
3892.7(5)	1.2(4)	1	0.071(14)	1.0	0.03(1)
4379.6(2)	2.44(29)	2	0.149(16)	1.0	0.11(1)
4413.9(3)	2.2(4)	2	0.099(14)	1.0	
4596.3(3)	0.84(15)	1	0.111(12)	1.0	0.09(2)
4804.0(4)	0.59(14)	1	0.100(12)	1.0	
4860.4(3)	1.10(19)	1	0.099(11)	1.0	
4922.5(2)	0.62(10)	1	0.36(4)	1.0	0.18(4)
4932.6(3)	0.68(18)	1	0.180(23)	1.0	0.09(4)
4948.4(6)	0.80(28)	1	0.121(25)	1.0	
4960.3(2)	0.68(17)	1	0.178(21)	1.0	
4979.9(1)	0.75(5)	1	1.00(7)	1.0	0.79(26)
5011.8(1)	0.77(7)	1	0.87(6)	1.0	0.54(6)
5059.4(3)	0.83(21)	1	0.085(15)	1.0	
5206.9(2)	0.82(13)	1	0.246(24)	1.0	
5224.9(4)	0.72(17)	1	0.114(24)	1.0	
5282.7(2)	0.70(14)	1	0.222(24)	1.0	0.16(12)
5316.0(3)	0.76(16)	1	0.125(21)	1.0	
5358.9(5)	1.1(3)	1	0.063(17)	1.0	
5365.8(6)	0.88(25)	1	0.049(18)	1.0	0.08(6)
5398.1(3)	0.69(15)	1	0.234(26)	1.0	0.16(4)
5431.9(6)	0.65(17)	1	0.24(3)	1.0	
5464.7(4)	0.56(16)	1	0.38(4)	1.0	
5601.2(3)	1.06(22)	1	0.184(24)	1.0	
5635.5(3)	1.1(4)	1	0.060(18)	1.0	
5674.2(3)	0.86(17)	1	0.212(27)	1.0	0.22(4)
5694.7(4)	1.01(25)	1	0.161(25)	1.0	
5734.0(1)	0.72(5)	1	1.24(9)	1.0	
5776.3(2)	0.90(8)	1	0.73(5)	1.0	0.91(13)
5792.4(4)	0.78(20)	1	0.27(4)	1.0	0.33(7)
5812.3(3)	0.83(18)	1	0.25(3)	1.0	0.17(14)
5827.5(1)	0.76(8)	1	0.80(6)	1.0	0.8(10)
5837.0(2)	0.80(17)	1	0.28(4)	1.0	0.37(6)
5852.6(4)	1.0(4)	1	0.172(22)	1.0	
5878.1(2)	0.76(12)	1	0.26(3)	1.0	0.28(6)
5890.1(1)	0.77(10)	1	0.38(4)	1.0	0.35(6)
5908.8(3)	0.83(17)	1	0.25(3)	1.0	
5918.4(5)	1.03(27)	1	0.122(18)	1.0	
5940.4(1)	0.76(6)	1	0.94(7)	0.84(4)	0.82(30)
5966.9(1)	0.75(8)	1	0.61(5)	1.0	0.58(8)
5980.3(1)	0.77(7)	1	0.99(8)	1.0	1.11(14)
5995.9(7)	0.62(23)	1	0.16(4)	1.0	0.18(12)
6008.9(3)	0.75(14)	1	0.35(4)	1.0	0.32(6)
6019.4(3)	0.86(13)	1	0.231(24)	1.0	0.46(23)
6055.9(2)	0.93(10)	1	0.241(21)	1.0	0.24(7)
6064.9(3)	0.81(12)	1	0.270(28)	1.0	0.31(8)
6078.8(6)	0.90(19)	1	0.176(29)	1.0	0.28(8)
6084.1(4)	0.83(15)	1	0.217(29)	1.0	0.30(8)
6108.2(3)	1.10(14)	1	0.47(5)	1.0	0.20(14)
6147.9(3)	0.98(12)	1	0.57(5)	1.0	0.49(12)
6159.1(5)	0.50(9)	1	0.43(5)	0.65(9)	0.43(12)
6193.8(3)	0.8(3)	1	0.062(20)	1.0	0.27(16)
6211.0(3)	0.87(16)	1	0.21(3)	1.0	0.28(17)

TABLE I. (*Continued.*)

$E_x^a$ (keV)	$W(90^\circ)/$ $W(127^\circ)$	$J$	$\Gamma_0^2/\Gamma^b$ (eV)	$\Gamma_0/\Gamma$	$\Gamma_0^2/\Gamma^c$ (eV)
6229.1(3) <sup>d</sup>	1.1(3)	1	0.144(25)	1.0	0.32(9)
6252.7(2)	0.62(15)	1	0.23(3)	1.0	0.46(10)
6276.1(4)	1.04(21)	1	0.114(16)	1.0	0.35(11)
6293.3(4)	0.77(15)	1	0.143(17)	1.0	
6308.0(2)	0.74(10)	1	0.41(4)	1.0	
6322.8(2)	1.01(13)	1	0.38(4)	1.0	0.96(23)
6360.4(3)	0.57(11)	1	0.22(3)	1.0	
6410.2(2)	0.86(9)	1	0.328(27)	1.0	0.48(21)
6456.8(2)	0.83(10)	1	0.31(4)	1.0	0.41(17)
6468.1(4) <sup>e</sup>	0.68(12)	1	0.24(3)	1.0	0.38(20)
6492.5(3)	1.05(14)	1	0.202(21)	1.0	
6501.9(2)	0.75(9)	1	0.274(25)	1.0	
6546.4(3)	0.91(12)	1	0.215(22)	1.0	
6568.5(3)	1.04(13)	1	0.189(21)	1.0	
6627.9(1)	0.81(10)	1	0.54(5)	1.0	
6681.9(2)	0.83(10)	1	0.63(5)	1.0	
6705.8(3)	0.79(11)	1	0.37(3)	1.0	
6721.4(1)	0.81(7)	1	1.16(9)	1.0	
6765.0(3)	0.70(12)	1	0.65(7)	1.0	
6793.8(4)	1.13(26)	1	0.16(4)	1.0	
6820.4(3)	0.70(12)	1	0.52(6)	1.0	
6851.3(3)	0.88(16)	1	0.36(5)	1.0	
6872.9(4)	0.53(20)	1	0.24(4)	1.0	
6900.6(3)	0.76(10)	1	0.36(4)	1.0	
6911.6(5)	0.94(18)	1	0.201(29)	1.0	
6969.1(2)	0.73(6)	1	0.91(8)	0.63(4)	
6991.8(5)	0.8(4)	1	0.11(3)	1.0	
7013.3(2)	0.85(8)	1	0.52(4)	1.0	
7025.2(2)	0.74(6)	1	0.87(6)	1.0	
7038.8(4)	0.76(13)	1	0.229(28)	1.0	
7064.2(4)	1.02(12)	1	0.33(3)	1.0	
7079.3(3)	1.03(10)	1	0.44(4)	1.0	
7097.9(3)	0.67(10)	1	0.35(3)	1.0	
7118.5(1)	0.75(5)	1	1.23(9)	1.0	
7128.7(2)	0.78(7)	1	0.78(6)	1.0 <sup>f</sup>	
7141.0(3)	0.71(9)	1	0.42(4)	1.0	
7155.1(4)	0.54(10)	1	0.31(3)	1.0	
7223.5(3)	0.90(8)	1	0.67(5)	1.0	
7233.7(3)	1.05(10)	1	0.57(5)	1.0	
7270.3(2)	0.91(7)	1	0.99(8)	1.0	
7279.7(1)	0.81(5)	1	2.78(19)	0.90(3)	
7304.1(2)	0.81(7)	1	0.77(6)	1.0	
7327.3(2)	0.89(7)	1	0.93(7)	1.0	
7353.8(4)	0.95(12)	1	0.33(3)	1.0	
7367.7(5)	0.91(14)	1	0.29(3)	1.0 <sup>g</sup>	
7398.4(2)	0.86(7)	1	0.90(7)	1.0	
7409.8(5)	1.18(15)	1	0.31(3)	1.0	
7430.2(2)	0.87(7)	1	0.79(6)	0.60(3)	
7455.2(3)	0.87(8)	1	0.59(5)	1.0	
7535.6(2)	0.72(6)	1	0.93(7)	1.0	
7551.6(3)	0.68(9)	1	0.47(4)	0.34(3)	
7569.3(3)	0.63(8)	1	0.51(4)	1.0	
7660.1(4)	0.64(11)	1	0.34(4)	1.0	
7679.2(5)	0.72(13)	1	0.30(4)	0.36(5)	
7706.8(3)	0.86(9)	1	0.60(5)	1.0	
7721.4(2)	0.60(6)	1	0.71(6)	1.0	
7743.3(3)	0.59(8)	1	0.50(4)	1.0	

TABLE I. (*Continued.*)

$E_x^a$ (keV)	$W(90^\circ)/$ $W(127^\circ)$	$J$	$\Gamma_0^2/\Gamma^b$ (eV)	$\Gamma_0/\Gamma$	$\Gamma_0^2/\Gamma^c$ (eV)
7760.9(4)	0.64(9)	1	0.42(4)	0.65(7)	
7778.0(2)	0.69(6)	1	0.93(7)	1.0	
7794.7(5)	0.85(14)	1	0.27(3)	1.0	
7830.5(4)	0.67(9)	1	0.34(3)	1.0	
7841.0(5)	0.83(11)	1	0.40(4)	0.51(5)	
7853.0(5)	0.68(11)	1	0.32(4)	1.0	
7883.0(5)	0.63(11)	1	0.33(4)	1.0	
7894.8(7)	0.84(17)	1	0.23(3)	1.0	
7909.4(4)	0.63(9)	1	0.40(4)	1.0	
7951.5(3)	0.78(9)	1	0.52(5)	0.44(3)	
7970.6(4)	0.98(13)	1	0.35(4)	1.0	
7988.9(4)	0.63(10)	1	0.37(4)	1.0	
8033.2(4)	0.80(11)	1	0.34(4)	1.0	
8060.8(3)	0.94(10)	1	0.47(4)	1.0	
8087.6(3)	0.70(7)	1	0.61(5)	0.31(2)	
8113.0(5)	0.50(9)	1	0.32(3)	1.0	
8125.4(4)	0.59(9)	1	0.39(4)	1.0	
8145.7(4)	0.48(9)	1	0.35(4)	1.0	
8161.0(3)	0.77(9)	1	0.51(4)	1.0	
8177.1(5)	0.50(10)	1	0.34(4)	1.0	
8189.1(4)	0.66(9)	1	0.40(4)	1.0	
8255.5(4)	0.73(12)	1	0.32(3)	1.0	
8277.0(4)	0.53(8)	1	0.42(4)	1.0	
8304.0(3)	0.79(9)	1	0.49(4)	1.0	
8316.6(4)	0.78(9)	1	0.54(5)	1.0	
8327.3(7)	0.90(16)	1	0.24(3)	1.0	

<sup>a</sup>The peak fitting error in parenthesis is given in units of the last digit. This energy was deduced from the  $\gamma$ -ray energy measured at  $127^\circ$  to the beam.

<sup>b</sup>This work. The statistical and systematic uncertainties (associated with strength normalization, photon flux, and efficiency) are reflected in the errors. Although levels up to  $E_x \approx 5.5$  MeV are possibly fed by higher-energy levels, the effect of the feeding is not considered.

<sup>c</sup>Values taken from [27].

<sup>d</sup>This transition is known from previous work [27] and coincides with a possible branch of the state at 7129 keV.

<sup>e</sup>This transition is known from previous work [27] and coincides with a possible branch of the state at 7368 keV.

<sup>f</sup>Possible branch to the  $2_1^+$  state coincides with the transition at 6229 keV.

<sup>g</sup>Possible branch to the  $2_1^+$  state coincides with the transition at 6468 keV.

where  $\Gamma_0$  is given in units of meV and  $E_\gamma$  in units of MeV. From the present work, the total  $E1$  strength of  $\Sigma B(E1) \uparrow = 0.613(6) e^2 \text{ fm}^2$  below  $E_x = 8.327$  MeV was obtained assuming  $E1$  nature for the observed dipole transitions. If one would assume  $M1$  strengths in  $^{204}\text{Pb}$  comparable to  $^{206}\text{Pb}$  [12] and  $^{208}\text{Pb}$  [42], then the results on the total  $E1$  strength would change by at most 10%. Therefore, it would not affect the conclusion on the gross properties of the  $E1$  strength distribution discussed below. The present total  $E1$  strength corresponds to 0.546(6)% of the energy-weighted TRK sum rule value, which can be compared to the values of 0.79(1)% for  $^{206}\text{Pb}$  [43], 0.35(2)% for  $^{207}\text{Pb}$  [44], and 1.01(6)% for  $^{208}\text{Pb}$  [42].

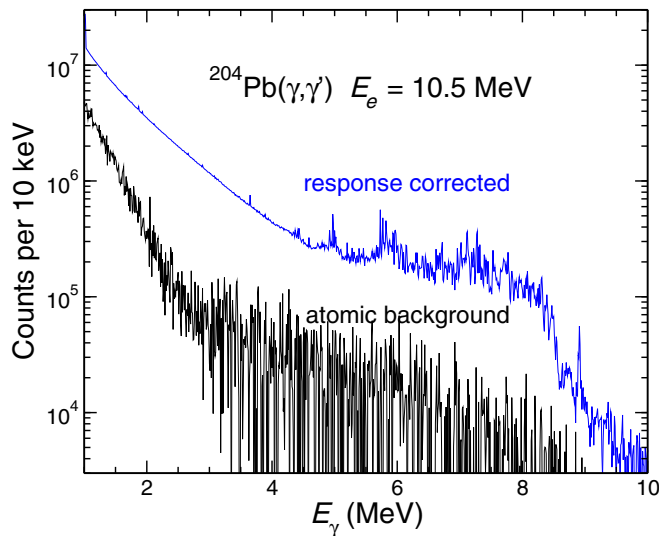


FIG. 3. Spectrum of the two detectors at  $127^\circ$ , corrected for detector response (blue), and simulated spectrum of photons scattered from the target to the detectors by atomic processes (black).

### B. Determination of the dipole-strength distribution

The determination of the dipole-strength distribution and the related photoabsorption cross section requires the knowledge of the intensity distribution of the ground-state transitions and their branching ratios. As these cannot be derived directly from the measured spectra, we applied statistical methods to discriminate between  $\gamma$  rays from nuclear excitations and photons scattered by atomic processes and to disentangle the intensity distributions of elastic and inelastic transitions in the quasicontinuum of nuclear levels.

First, a spectrum of the ambient background adjusted to the intensities of the transitions from  $^{40}\text{K}$  and  $^{208}\text{Tl}$  decay in the in-beam spectrum was subtracted from the measured spectrum. To correct the measured spectrum for the detector response, spectra of monoenergetic  $\gamma$  rays were calculated in steps of 10 keV by using the simulation code GEANT4. Starting from the high-energy end of the experimental spectrum, the simulated spectra were subtracted sequentially (spectrum-stripping method [45]).

The background radiation produced by atomic processes in the  $^{204}\text{Pb}$  target was obtained from a GEANT4 simulation. The simulation contains the detector crystals and housings, the BGO shields, the beam tube, and detector shielding. As it is not included other components such as detector stands, cooling systems, etc., one cannot expect a perfect description, in particular not at low energies in the intense region of backscattering and annihilation peaks. This is, however, not critical for the determination of the cross sections at higher energy as described in the following. The calculated atomic background is compared with the response-corrected spectrum in Fig. 3. The atomic background amounts in average to only a few percentages of the intensity in the spectrum and approaches it above the neutron threshold, which corresponds to the behavior found in previous studies, e.g., in Refs. [30,43,46–48]. The intensity in the experimental spec-

trum above the atomic background contains a considerable amount of nuclear strength in a quasicontinuum, which is formed by a large number of unresolved transitions with small intensities according to the increasing nuclear level density at high energy in combination with the finite detector resolution. Because of the different orders of magnitude, the nuclear intensity distribution resulting from the subtraction of the simulated atomic background is not very sensitive to uncertainties of the latter, for which we assume 5%. The nuclear intensity distribution contains ground-state (elastic) transitions and, in addition, branching (inelastic) transitions to lower-lying excited states as well as transitions from those states to the ground state (cascade transitions). The different types of transitions cannot be clearly distinguished. However, for the determination of the photoabsorption cross section and the partial widths  $\Gamma_0$ , the intensities of the ground-state transitions are needed. Therefore, contributions of inelastic and cascade transitions have to be subtracted from the spectra. We corrected the intensity distributions by simulating  $\gamma$ -ray cascades from the levels in the entire energy region using the code  $\gamma$ DEX [49,50]. This code works analogously to the strategy of the code DICEBOX [51] developed for  $(n, \gamma)$  reactions, but in addition it includes also the excitation from the ground state. In the present simulations, level schemes (nuclear realizations) including states with  $J = 0, \dots, 5$  were created for energy bins of 10 keV, which describe statistical averages for a number of states in the bins resulting from calculated level densities. Below about 3 MeV, where the level density is too low for the statistical approach, known low-lying levels were taken into account by filling the respective bins and deriving the level density from the number of levels in a bin. The level densities in the statistical region at higher energy were calculated by using the constant-temperature model [52] with the parameters  $T = 0.73(3)$  MeV and  $E_0 = -0.24(6)$  MeV adjusted to experimental level densities [53]. In the individual nuclear realizations, the values of  $T$  and  $E_0$  were varied randomly within a Gaussian distribution with a standard deviation corresponding to the uncertainties given in Ref. [53]. The parity distribution of the level densities was modeled according to the information given in Ref. [54]. Partial widths were varied in the individual nuclear realizations applying the Porter-Thomas distribution [55].

The first inputs for the photon strength function simulations were assumed to be Lorentz-shaped. For the  $E1$  strength, a sum of three Lorentz functions that account for a triaxial deformation of the nucleus was used with parameters described in Refs. [56,57]. In the present case, deformation parameters of  $\beta_2 = 0.008$  [58] and  $\gamma = 0$  [59] were applied. The parameters for the  $M1$  and  $E2$  strengths were taken from global parametrizations of  $M1$  spin-flip resonances and  $E2$  isoscalar resonances, respectively [60]. Low-lying levels were also taken into account. Spectra of  $\gamma$ -ray cascades were generated for groups of levels in energy bins of  $\Delta E = 100$  keV. Starting from the high-energy end of the intensity distribution, that contains ground-state transitions only, the simulated intensities of the ground-state transitions were normalized to the experimental ones in the considered bin. The intensity distribution of the branching transitions was subtracted from the total intensity distribution. Applying this procedure step

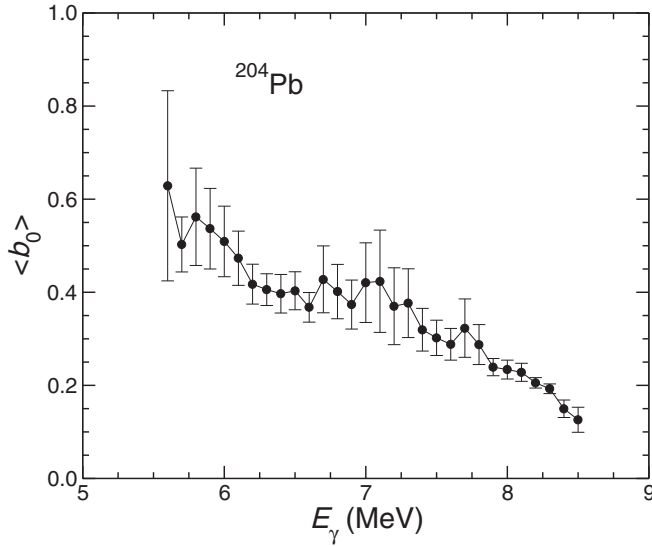


FIG. 4. Average branching ratios of ground-state transitions resulting from the simulations of statistical  $\gamma$ -ray cascades up to  $S_n$  as described in the text.

by step for each energy bin moving toward the low-energy end of the spectrum, one obtains the intensity distribution of the ground-state transitions. Simultaneously, the branching ratios  $b_0(E)$  of the ground-state transitions are determined for each energy bin. In an individual nuclear realization, the branching ratio  $b_0(E)$  is calculated as the ratio of the sum of the intensities of the ground-state transitions from all levels in  $\Delta E$  to the total intensity of all transitions depopulating those levels to either any low-lying energy bin or to the ground state [43,48,50,61–63]. Branching ratios  $\langle b_0(E) \rangle$ , averaged over the many nuclear realizations in the present cascade simulations, are illustrated in Fig. 4.

The uncertainty of the number of counts  $N(E)$  in an energy bin of the experimental intensity distribution was deduced as

$$\delta N(E) = \sqrt{N(E)} + \sum_{E'} [\sqrt{N(E' > E)} b(E' \rightarrow E)], \quad (4)$$

where  $b(E' \rightarrow E)$  is the branching intensity from bin  $E'$  to bin  $E$ . We transform  $N(E)$  to the scattering cross section according to

$$\sigma_{\gamma\gamma}(E) = N(E)/[\epsilon(E) \Phi_\gamma(E) W(E) N_N \Delta t \Delta E] \quad (5)$$

with the quantities defined in Eq. (1), the absolute detector efficiency  $\epsilon(E)$ , the measuring time  $\Delta t$ , and the bin width  $\Delta E$ . The absorption cross section in each bin is obtained as  $\sigma_\gamma(E) = \sigma_{\gamma\gamma}(E)/b_0(E)$  for each nuclear realization. Finally, the absorption cross sections of each bin were obtained by averaging over the values of the individual nuclear realizations.

The simulations were performed iteratively, where the strength function obtained from an iteration step was used as the input for the next step. We note that the simulations are little sensitive to the shape of the first input strength function, which was tested, for example, in Refs. [8,49]. The iteration is stopped when the input strength function and the output strength function were in agreement within their respective

TABLE II. Photoabsorption cross section of  $^{204}\text{Pb}$  deduced from the present ( $\gamma, \gamma'$ ) experiment.

$E_\gamma$ (MeV)	$\sigma$ (mb) <sup>a</sup>
5.5	6(5)
5.7	13(6)
5.8	17(5)
5.9	16(4)
6.0	17(4)
6.1	16(4)
6.2	14(3)
6.3	17(3)
6.4	16(3)
6.5	18(4)
6.6	21(4)
6.7	24(5)
6.8	24(4)
6.9	21(4)
7.0	27(5)
7.1	37(7)
7.2	36(5)
7.3	39(6)
7.4	33(5)
7.5	34(4)
7.6	33(4)
7.7	41(4)
7.8	36(4)
7.9	38(3)
8.0	34(3)
8.1	37.7(29)
8.2	38.9(27)
8.3	41.9(27)
8.4	32.5(22)
8.5	30.1(19)

<sup>a</sup>Absorption cross section resulting from the experimental intensity distribution including the quasicontinuum, corrected for branching intensities and branching ratios obtained from  $\gamma$ -ray cascade simulations. The uncertainties include statistical uncertainties of the spectra (see Sec. III B), the given uncertainties of the efficiencies and the subtracted simulated background spectra, uncertainties of the flux resulting from the integrated cross sections of the  $^{11}\text{B}$  levels and the given uncertainties of the level-density parameters.

uncertainties. This was achieved after the sixth iteration in the present case.

Toward low energy, the uncertainties increase due to the use of the spectrum-stripping method and the strength functions do not converge. Besides, the assumption of a statistical quasicontinuum becomes invalid and individual states become important. Therefore, the low-energy parts of the strength functions obtained from the individual iteration steps were replaced by the mentioned Lorentz curves as soon as the uncertainties of the values exceed 100%, and the combination of the Lorentz curve at low energy and the data at high energy resulting from the iteration was used as the input strength function for the next iteration step. We note that the methods described here were tested in several ways. In combined studies using ( $\gamma, \gamma'$ ) and ( $n, \gamma$ ) reactions, the strength functions obtained from the ( $\gamma, \gamma'$ ) experiments were used as

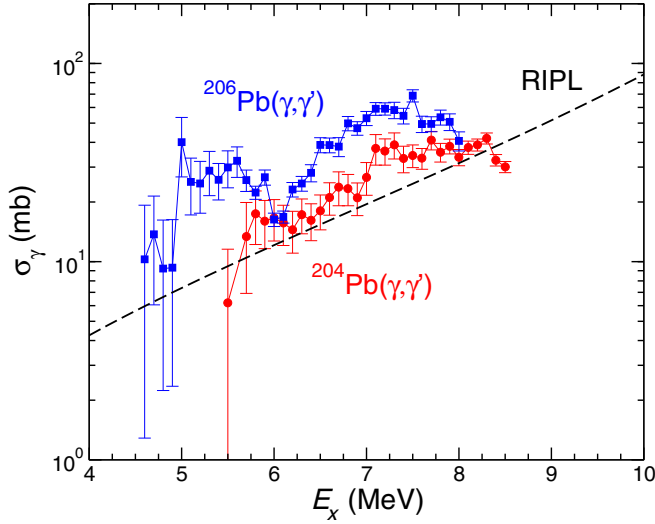


FIG. 5. Photoabsorption cross section of  $^{204}\text{Pb}$  resulting from the present  $(\gamma, \gamma')$  experiment (red circles) in comparison with that of  $^{206}\text{Pb}$  (blue squares) as taken from Ref. [43]. Also shown is the Lorentz curve from RIPL (black dashed line).

inputs for the analysis of the  $(n, \gamma)$  data and gave a consistent description [49,64,65]. The calculated branching ratios  $\langle b_0(E) \rangle$  proved to be compatible with experimental values obtained from experiments with quasimonoeenergetic photon beams [50,66].

The final absorption cross sections as obtained from the last iteration steps are listed in Table II and graphed in Fig. 5. The uncertainties of the cross-section values include statistical uncertainties of the spectrum, the given uncertainties of the efficiency and the subtracted simulated background spectrum, uncertainties of the flux resulting from the integrated cross sections of the  $^{11}\text{B}$  levels and the uncertainties of the level-density parameters given in the text above. Systematic uncertainties of level-density models can result in additional uncertainties of up to about 20%, which are not included here. Such deviations of modeled from experimentally determined level densities and between the various level-density models are, for example, discussed in Ref. [67].

#### IV. DISCUSSION

The experimental data of  $^{204}\text{Pb}$  obtained in the present NRF measurement shows unique character of the low-lying dipole strength distribution. In Fig. 5, the photoabsorption

cross section of  $^{204}\text{Pb}$  deduced from the quasicontinuum analysis is compared with that of  $^{206}\text{Pb}$  [43] and a Lorentz curve taken from the database Reference Input Parameter Library (RIPL) [60]. It can be seen that the cross sections include extra strength with respect to the RIPL curve, which might be considered as the PDR. The cross section values in  $^{204}\text{Pb}$  is approximately 60% of that in  $^{206}\text{Pb}$  in the energy range from 6 to 8 MeV. This difference is consistent with the total strengths obtained from the analysis of the resolved peaks, i.e.,  $\Sigma B(E1) \uparrow = 0.339(5) e^2 \text{ fm}^2$  for  $^{204}\text{Pb}$  and  $0.516(9) e^2 \text{ fm}^2$  for  $^{206}\text{Pb}$  in the same energy range, which may support that there are stronger single-particle excitations in  $^{206}\text{Pb}$  than  $^{204}\text{Pb}$ .

In the following, theoretical investigations of the spectral distributions of low-lying dipole excited states in the semimagic  $^{204}\text{Pb}$  nucleus and their relation to the PDR were conducted with the EDF theory and the three-phonon QPM [15,17,18].

#### A. Theoretical model

An important advantage of the EDF+QPM approach is the description of the excited-state wave functions in terms of QRPA phonons which are defined [68] by the equation:

$$Q_{\lambda\mu}^+ = \frac{1}{2} \sum_{jj'} [\psi_{jj'}^{\lambda i} A_{\lambda\mu}^+(jj') - \phi_{jj'}^{\lambda i} \tilde{A}_{\lambda\mu}(jj')], \quad (6)$$

where  $j \equiv (nljm\tau)$  is a single-particle proton or neutron state;  $A_{\lambda\mu}^+$  and  $\tilde{A}_{\lambda\mu}$  are time-forward and time-backward operators, coupling two-quasiparticle creation or annihilation operators to a total angular momentum  $\lambda$  with projection  $\mu$  by means of the Clebsch-Gordan coefficients  $C_{jmj'm'}^{\lambda\mu} = \langle jmj'm' | \lambda\mu \rangle$ . The excitation energies of the phonons and the time-forward and time-backward amplitudes  $\psi_{j_1j_2}^{\lambda i}$  and  $\phi_{j_1j_2}^{\lambda i}$  in Eq. (6) are determined by solving QRPA equations [68]. QRPA is also commonly called the ‘‘quasiboson’’ approximation, as QRPA phonons are associated with pure bosonic states [69]. In the QPM the phonon operators satisfy commutation relations which take into account the internal fermionic structure of the phonons, thus satisfying the Pauli principle. Furthermore, the QRPA phonons are used as building blocks of the three-phonon QPM model configuration space [68,70], which provides a microscopic way to multiconfigurational mixing. For spherical even-even nuclei, the model Hamiltonian is diagonalized on an orthonormal set of wave functions constructed from one-, two-, and three-phonon configurations:

$$\Psi_\nu(JM) = \left\{ \sum_i R_i(J\nu) Q_{JM}^+ + \sum_{\substack{\lambda_1 i_1 \\ \lambda_2 i_2}} P_{\lambda_2 i_2}^{\lambda_1 i_1}(J\nu) [Q_{\lambda_1 \mu_1 i_1}^+ \times Q_{\lambda_2 \mu_2 i_2}^+]_{JM} + \sum_{\substack{\lambda_1 i_1 \lambda_2 i_2 \\ \lambda_3 i_3}} T_{\lambda_3 i_3}^{\lambda_1 i_1 \lambda_2 i_2}(J\nu) [(Q_{\lambda_1 \mu_1 i_1}^+ \otimes Q_{\lambda_2 \mu_2 i_2}^+)_{IK} \otimes Q_{\lambda_3 \mu_3 i_3}^+]_{JM} \right\} \Psi_0, \quad (7)$$

where  $R$ ,  $P$ , and  $T$  are unknown amplitudes, and  $\nu$  labels the number of the excited states.

The nature of nuclear excitation can be studied by examining the spatial structure of the transition. This is achieved by

analyzing the one-body transition densities,  $\delta\rho(r)$ , which are related to the nondiagonal elements of the one-body nuclear density matrix [17,18]. By analyzing the transition density spatial pattern we obtain a very detailed picture, for example, of the radial distribution and localization of the excitation process. The electromagnetic transition matrix elements are calculated for transition operators including the interaction of quasiparticles and phonons [69] where exact commutation relations are implemented which is a necessary condition in order to satisfy the Pauli principle.

### B. Comparison with the experimental results

Consistent with previous investigations of  $E1$  strength in various nuclei [12,17,18,71,72], the present QPM calculations are performed with single-particle energies obtained in a self-consistent manner from EDF approach linked to fully self-consistent Hartree-Fock-Bogoliubov calculations. The excited states are calculated with a residual interaction represented in separable form with strength parameters fixed empirically [18]. As a further advantage over other QRPA models, the QPM approach incorporates a multiphonon model space built of natural and unnatural parity states. Here, the model basis is constructed of one-, two-, and three-phonon (microscopically described) configurations with  $J^\pi = 1^\pm, 2^+, 3^-, 4^+, 5^-, 6^+,$  and  $7^-$  and excitation energies in agreement with the range of the present NRF experiment. The QRPA and QPM calculations in  $^{204}\text{Pb}$  shown here follow the model approach and methodology outlined in our previous studies of the dipole response in  $^{206}\text{Pb}$  and  $^{208}\text{Pb}$  [12,71]. In particular, the total dipole photoabsorption cross section and the GDR properties obtained from the present QRPA calculations for  $^{204}\text{Pb}$  are consistent with these previous results. Since QRPA one-phonon configurations up to  $E_x = 35$  MeV are considered, the GDR nuclear polarization contributions to the  $E1$  transitions of the low-lying  $1^-$  states are explicitly taken into account. There is therefore no need to introduce additional effective charges.

In QRPA theory, the one-phonon transition density is given by a coherent sum over two-quasiparticle transition densities that are incorporated in the structure of a QRPA phonon defined with Eq. (6). The shape of the transition density is strongly correlated with the collectivity of the phonon [17]. Typically, the transition densities of noncollective two-quasiparticle excitations have pronounced peaks within the nucleus [73]. In contrast, those corresponding to the collective transitions with a large number of coherently contributing two-quasiparticle transitions have a maximum at the nuclear surface. Thus, the proton and neutron transition densities of the individual QRPA  $1^-$  states located in the energy range  $E_x \approx 6.5\text{--}7.5$  MeV in  $^{204}\text{Pb}$ , shown in Fig. 6 (upper panel), can be associated with an intermediate behavior between the collective neutron skin oscillation and the single-particle excitation. The transition densities retain the single-particle origin of neutron oscillations at the nuclear surface, but also include additional collective dynamical effects associated with the coherent excitation of a sequence of neutron single-particle states [17,18,71,72].

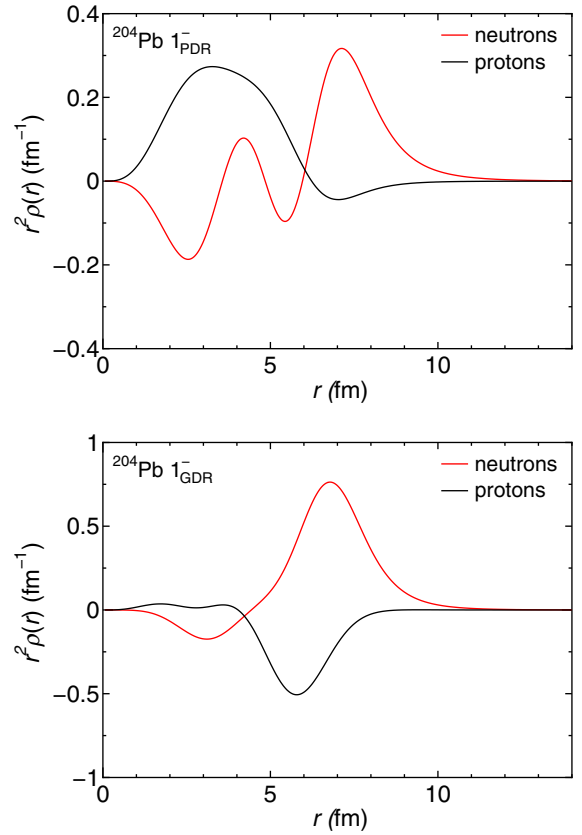


FIG. 6. (Top) Summed neutron and proton transition densities of the  $[1_{\text{PDR}}^-]$  states and (bottom) the same for the  $[1_{\text{GDR}}^-]$  states obtained from QRPA calculations in  $^{204}\text{Pb}$ .

The defining characteristic of the PDR neutron transition density is the nodal structure [17,18]. In particular, the radial transition form factors correspond to a classical droplet wobbling mode in which matter is oscillating in radial direction as a standing compression surface wave. In quantum nuclear systems, the PDR skin modes correspond to a diffusivity oscillation, very different from the collective modes like the GDR shown in Fig. 6 (bottom panel). The theoretical calculations of neutron and proton transition densities confirm the unique character of the low-lying  $1^-$  states in  $^{204}\text{Pb}$ . Theoretically, the description of the spectral distribution of the low-lying dipole strength and the fine structure of nuclear excitations requires to couple the  $1^-$  one-phonon QRPA doorway states to more complex configurations which, in turn, are coupled again to other configurations. This coupling causes a fragmentation and a shift of the low-lying  $E1$  strength toward lower energy which is achieved in a EDF+three-phonon QPM approach [18].

In Figs. 7(a) and 7(b), the experimental  $B(E1)\uparrow$  values are compared with the EDF+QPM calculations. The total measured  $B(E1)\uparrow$  value up to  $E_x = 8.327$  MeV amounts to  $\Sigma B(E1)\uparrow = 0.613(6) e^2 \text{fm}^2$ . The corresponding QPM value above the experimental sensitivity limits is  $\Sigma B(E1)\uparrow = 0.971 e^2 \text{fm}^2$ . Overall, the theoretical results in  $^{204}\text{Pb}$  agree with the experiment, with respect to the total  $B(E1)\uparrow$  strength and with the TRK value. The total  $B(E1)\uparrow$  strength located

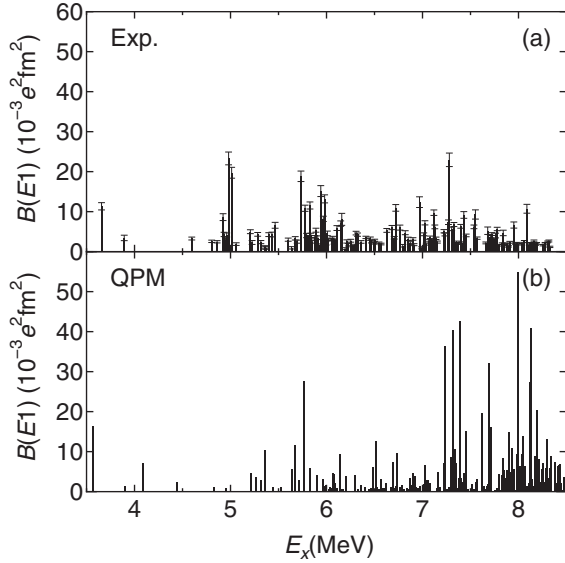


FIG. 7.  $B(E1)\uparrow$  values deduced from the present NRF experiment (a) and the same for the EDF+QPM calculations (b) in  $^{204}\text{Pb}$ .

below  $E_x \approx 8.4$  MeV obtained by the experiment and the EDF+QPM approach exhausts approximately 0.6% and 1%, respectively. The QPM spectrum which spreads at excitation energy larger than  $\approx 7$  MeV indicates larger  $E1$  strength than the one experimentally observed. This suggests that a part of the  $E1$  strength is hidden in the continuous background of the observed NRF spectra and branching ratios are smaller than unity. This is supported by the results of the quasicontinuum analysis shown in Figs. 4 and 5. In addition, considering that the present three-phonon QPM calculations and model configuration spaces of two- and three-phonon configurations are bound in the energy range of the performed NRF experiment, this truncation can affect the coupling to the higher-lying  $1^-$  excited states that are located outside of these constraints. As a result, the QPM calculations underestimate the statistical model simulations for the quasicontinuum contribution in the total transition strength below  $E_x = 8.4$  MeV as shown in Fig. 8. To understand this, we additionally performed two-phonon QPM calculations in a model configuration space extended by about 1 MeV for the two-phonon components, which showed that the contribution from higher-lying one-phonon  $1^-$  states outside the energy range of the NRF experiment may have important consequences and be a possible reason for this reduction in total  $E1$  strength. From the extended two-phonon QPM calculations, we found about twice the  $E1$  absorption cross section below  $E_x = 8.4$  MeV (see Fig. 8), which is associated with the increase in fragmentation toward lower energies of one-phonon  $1^-$  states mostly located at  $E_x \approx 9$ –10 MeV and belonging to low-energy GDR. These theoretical observations greatly improve the comparison with the experimental results including the quasicontinuum contribution. We also point out that the above differences are not a matter of the interaction parameters but may originate in the quasiparticle spectrum which indicates a stronger coupling to low-energy GDR.

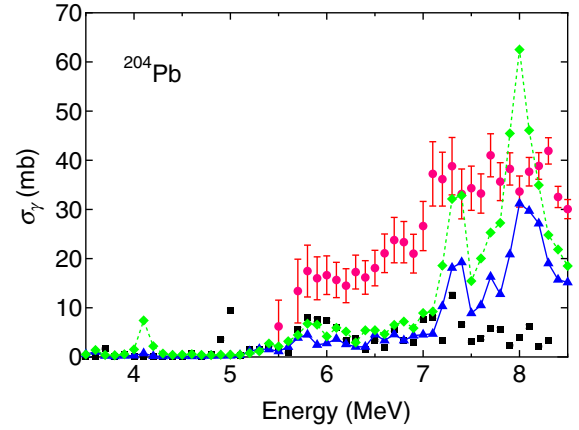


FIG. 8. Experimental  $\gamma$ -ray absorption cross sections derived from resolved peaks (squares) and from the quasicontinuum analysis (red circles), averaged over energy bins of 100 keV. Also shown are cross sections predicted by EDF+three-phonon QPM calculations confined in the NRF energy domain (blue triangles) and extended EDF+two-phonon QPM (green diamonds) calculations, smeared by the Lorentzian width of 100 keV. Lines are drawn to guide the eye.

By comparing the QRPA to the multiphonon EDF+QPM calculations we find that the pure two-quasiparticles  $E1$  QRPA strength below the neutron threshold in  $^{204}\text{Pb}$  is strongly fragmented over many  $1^-$  excited states. Of particular interest are the QPM lowest-lying  $1_1^-$  at  $E_x(\text{QPM}) = 3.566$  MeV and  $1_2^-$  at  $E_x(\text{QPM}) = 3.903$  MeV states which are without QRPA counterpart because they contain a two-phonon quadrupole-octupole  $[2_1^+ \otimes 3_1^-]$  configuration, which accounts for  $\approx 50\%$  of the  $1_1^-$  and  $\approx 25\%$  of the  $1_2^-$  QPM wave function, respectively. The theoretical  $B(E1)\uparrow$  values of these  $1^-$  states are  $B(E1, \text{g.s.} \rightarrow 1_1^-)_{\text{QPM}} = 16 \times 10^{-3} e^2 \text{fm}^2$  and  $B(E1, \text{g.s.} \rightarrow 1_2^-)_{\text{QPM}} = 1.3 \times 10^{-3} e^2 \text{fm}^2$ . The experimentally observed dipole states located at  $E_x = 3.656$  and  $3.892$  MeV with  $B(E1)\uparrow = 11.3(9) \times 10^{-3}$  and  $3.4(7) \times 10^{-3} e^2 \text{fm}^2$ , respectively, may correspond to these predicted  $1^-$  states.

## V. SUMMARY

The dipole strength distribution in  $^{204}\text{Pb}$  up to the neutron separation energy has been studied in a photon scattering experiment at the ELBE bremsstrahlung facility by using an electron beam at a kinetic energy of 10.5 MeV. We identified 134  $J = 1$  and 2  $J = 2$  resonantly excited states below 8.4 MeV. The intensity distribution obtained from the measured spectra after a correction for detector response and a subtraction of atomic background in the target contains a quasicontinuum in addition to resolved peaks. Simulations of statistical  $\gamma$ -ray cascades have been performed to estimate the intensities of inelastic transitions and the branching ratios of the ground-state transitions. The experimental results were used to investigate the low-lying  $E1$  strength and compared with predictions from the self-consistent EDF

and the QPM. The EDF+QPM calculations reproduced the gross properties of the  $E1$  strength observed below the neutron separation energy in  $^{204}\text{Pb}$ . Analysis of the proton and neutron transition densities revealed that the low-lying  $E1$  strength is due to both the collective neutron skin oscillation and the single-particle excitation. However, more complex configurations due to coupling of  $1^-$  to multi-phonon states which causes a fragmentation and a shift of the low-lying  $E1$  strength toward lower energy were also observed.

## ACKNOWLEDGMENTS

We thank the staff of the ELBE accelerator facility for cooperation during the experiments, and A. Hartmann for the technical assistance. We also thank Y. Shibahara for the mass analysis of the target material. This work was supported in part by JSPS KAKENHI Grant No. 20K04007. N.T. was supported by the Romanian Ministry of Research and Innovation under contract PN 19 06 01 05.

- 
- [1] A. Bracco, E. Lanza, and A. Tamii, *Prog. Part. Nucl. Phys.* **106**, 360 (2019).
- [2] D. Savran, T. Aumann, and A. Zilges, *Prog. Part. Nucl. Phys.* **70**, 210 (2013).
- [3] A. Leistenschneider, T. Aumann, K. Boretzky, D. Cortina, J. Cub, U. Datta Pramanik, W. Dostal, Th. W. Elze, H. Emling, H. Geissel, A. Grünschloß, M. Hellstr, R. Holzmann, S. Ilievski, N. Iwasa, M. Kaspar, A. Kleinböhl, J. V. Kratz, R. Kulesa, Y. Leifels, E. Lubkiewicz *et al.* *Phys. Rev. Lett.* **86**, 5442 (2001).
- [4] N. Ryezayeva, T. Hartmann, Y. Kalmykov, H. Lenske, P. von Neumann-Cosel, V. Yu. Ponomarev, A. Richter, A. Shevchenko, S. Volz, and J. Wambach, *Phys. Rev. Lett.* **89**, 272502 (2002).
- [5] T. Hartmann, M. Babilon, S. Kamedzhiev, E. Litvinova, D. Savran, S. Volz, and A. Zilges, *Phys. Rev. Lett.* **93**, 192501 (2004).
- [6] P. Adrich, A. Klimkiewicz, M. Fallot, K. Boretzky, T. Aumann, D. Cortina-Gil, U. Datta Pramanik, Th. W. Elze, H. Emling, H. Geissel, M. Hellström, K. L. Jones, J. V. Kratz, R. Kulesa, Y. Leifels, C. Nociforo, R. Palit, H. Simon, G. Surówka, K. Sümmerer, and W. Waluś, *Phys. Rev. Lett.* **95**, 132501 (2005).
- [7] D. Savran, M. Fritzsche, J. Hasper, K. Lindenberg, S. Müller, V. Yu. Ponomarev, K. Sonnabend, and A. Zilges, *Phys. Rev. Lett.* **100**, 232501 (2008).
- [8] R. Schwengner, G. Rusev, N. Tsoneva, N. Benouaret, R. Beyer, M. Erhard, E. Grosse, A. R. Junghans, J. Klug, K. Kosev, H. Lenske, C. Nair, K. D. Schilling, and A. Wagner, *Phys. Rev. C* **78**, 064314 (2008).
- [9] O. Wieland, A. Bracco, F. Camera, G. Benzoni, N. Blasi, S. Brambilla, F. C. L. Crespi, S. Leoni, B. Million, R. Nicolini, A. Maj, P. Bednarczyk, J. Grebosz, M. Kmiecik, W. Meczynski, J. Styczen, T. Aumann, A. Banu, T. Beck, F. Becker *et al.*, *Phys. Rev. Lett.* **102**, 092502 (2009).
- [10] A. P. Tonchev, S. L. Hammond, J. H. Kelley, E. Kwan, H. Lenske, G. Rusev, W. Tornow, and N. Tsoneva, *Phys. Rev. Lett.* **104**, 072501 (2010).
- [11] R. Schwengner, R. Massarczyk, G. Rusev, N. Tsoneva, D. Bemmerer, R. Beyer, R. Hannaske, A. R. Junghans, J. H. Kelley, E. Kwan, H. Lenske, M. Marta, R. Raut, K. D. Schilling, A. Tonchev, W. Tornow, and A. Wagner, *Phys. Rev. C* **87**, 024306 (2013).
- [12] A. P. Tonchev, N. Tsoneva, C. Bhatia, C. W. Arnold, S. Goriely, S. L. Hammond, J. H. Kelley, E. Kwan, H. Lenske, J. Piekarewicz, R. Raut, G. Rusev, T. Shizuma, and W. Tornow, *Phys. Lett. B* **773**, 20 (2017).
- [13] M. N. Harakeh and A. van der Woude, *Giant Resonances: Fundamental High-frequency Modes of Nuclear Excitation* (Clarendon Press, Oxford, 2001).
- [14] N. Paar, D. Vretenar, E. Khan, and G. Colò, *Rep. Prog. Phys.* **70**, R02 (2007).
- [15] N. Tsoneva, H. Lenske, and Ch. Stoyanov, *Phys. Lett. B* **586**, 213 (2004).
- [16] N. Tsoneva and H. Lenske, *Phys. Lett. B* **695**, 174 (2011).
- [17] N. Tsoneva and H. Lenske, *Phys. Rev. C* **77**, 024321 (2008).
- [18] N. Tsoneva and H. Lenske, *Phys. At. Nucl.* **79**, 885 (2016).
- [19] J. Piekarewicz, *Phys. Rev. C* **73**, 044325 (2006).
- [20] J. Piekarewicz, *Phys. Rev. C* **83**, 034319 (2011).
- [21] T. Inakura and H. Nakada, *Phys. Rev. C* **92**, 064302 (2015).
- [22] X. Roca-Maza, X. Vinas, M. Centelles, B. K. Agrawal, G. Colo, N. Paar, J. Piekarewicz, and D. Vretenar, *Phys. Rev. C* **92**, 064304 (2015).
- [23] B. Alex Brown, *Phys. Rev. Lett.* **85**, 5296 (2000).
- [24] C. J. Horowitz and J. Piekarewicz, *Phys. Rev. Lett.* **86**, 5647 (2001).
- [25] R. Raut, A. P. Tonchev, G. Rusev, W. Tornow, C. Iliadis, M. Lugaro, J. Buntain, S. Goriely, J. H. Kelley, R. Schwengner, A. Banu, and N. Tsoneva, *Phys. Rev. Lett.* **111**, 112501 (2013).
- [26] N. Tsoneva, S. Goriely, H. Lenske, and R. Schwengner, *Phys. Rev. C* **91**, 044318 (2015).
- [27] J. Enders, P. von Brentano, J. Eberth, A. Fitzler, C. Fransen, R.-D. Herzberg, H. Kaiser, L. Käubler, P. von Neumann-Cosel, N. Pietralla, V. Yu. Ponomarev, A. Richter, R. Schwengner, and I. Wiedenhöver, *Nucl. Phys. A* **724**, 243 (2003).
- [28] R. Schwengner, R. Beyer, F. Dönau, E. Grosse, A. Hartmann, A. R. Junghans, S. Mallion, G. Rusev, K. D. Schilling, W. Schulze, and A. Wagner, *Nucl. Instrum. Methods A* **555**, 211 (2005).
- [29] R. Schwengner, G. Rusev, N. Benouaret, R. Beyer, M. Erhard, E. Grosse, A. R. Junghans, J. Klug, K. Kosev, L. Kostov, C. Nair, N. Nankov, K. D. Schilling, and A. Wagner, *Phys. Rev. C* **76**, 034321 (2007).
- [30] G. Rusev, R. Schwengner, F. Dönau, M. Erhard, E. Grosse, A. R. Junghans, K. Kosev, K. D. Schilling, A. Wagner, F. Bečvář, and M. Krtička, *Phys. Rev. C* **77**, 064321 (2008).
- [31] U. Kneissl, H. H. Pitz, and A. Zilges, *Prog. Part. Nucl. Phys.* **37**, 349 (1996); U. Kneissl, N. Pietralla, and A. Zilges, *J. Phys. G: Nucl. Part. Phys.* **32**, R217 (2006).
- [32] J. H. Kelley, E. Kwan, J. E. Purcell, C. G. Sheu, and H. R. Weller, *Nucl. Phys. A* **880**, 88 (2012).
- [33] F. Metzger, in *Progress in Nuclear Physics*, edited by O. Frisch (Pergamon Press, New York, 1959), Vol. 7, pp. 53–88.
- [34] S. Agostinelli *et al.*, *Nucl. Instrum. Methods A* **506**, 250 (2003).

- [35] E. Haug, *Radiat. Phys. Chem.* **77**, 207 (2008).
- [36] G. Roche, C. Ducos, and J. Proriot, *Phys. Rev. A* **5**, 2403 (1972).
- [37] F. Salvat, J. D. Martinez, R. Mayo, and J. Parellada, *Phys. Rev. A* **36**, 467 (1987).
- [38] G. Rusev, A. P. Tonchev, R. Schwengner, C. Sun, W. Tornow, and Y. K. Wu, *Phys. Rev. C* **79**, 047601 (2009).
- [39] R. Jenkins, R. W. Gould, and D. Gedke, *Quantitative X-ray Spectroscopy* (Dekker, New York, 1995).
- [40] E. Kwan, G. Rusev, A. S. Adekola, F. Dönau, S. L. Hammond, C. R. Howell, H. J. Karwowski, J. H. Kelley, R. S. Pedroni, R. Raut, A. P. Tonchev, and W. Tornow, *Phys. Rev. C* **83**, 041601(R) (2011).
- [41] R. Schwengner, R. Massarczyk, R. Beyer, M. Bhike, B. A. Brown, Krishichayan, K. Sieja, W. Tornow, D. Bemmerer, M. Butterling, V. Derya, M. Dietz, F. Fiedler, U. Friman-Gayer, A. Frotscher, M. Grieger, A. Hartmann, A. R. Junghans, T. Kögler, F. Ludwig, B. Lutz, H. Pai, T. Szücs, M. P. Takács, and A. Wagner, *Phys. Rev. C* **101**, 064303 (2020).
- [42] T. Shizuma, T. Hayakawa, H. Ohgaki, H. Toyokawa, T. Komatsubara, N. Kikuzawa, A. Tamii, and H. Nakada, *Phys. Rev. C* **78**, 061303(R) (2008).
- [43] T. Shizuma, N. Iwamoto, A. Makinaga, R. Massarczyk, R. Schwengner, R. Beyer, D. Bemmerer, M. Dietz, A. Junghans, T. Kögler, F. Ludwig, S. Reinicke, S. Schulz, S. Uraß, and A. Wagner, *Phys. Rev. C* **98**, 064317 (2018).
- [44] T. Shizuma, F. Minato, M. Omer, T. Hayakawa, H. Ohgaki, and S. Miyamoto, *Phys. Rev. C* **103**, 024309 (2021).
- [45] A. K. Furr, E. L. Robinson, and C. H. Robins, *Nucl. Instrum. Methods* **63**, 205 (1968).
- [46] R. Massarczyk, R. Schwengner, L. A. Bernstein, M. Anders, D. Bemmerer, R. Beyer, Z. Elekes, R. Hannaske, A. R. Junghans, T. Kögler, M. Röder, K. Schmidt, A. Wagner, and L. Wagner, *Phys. Rev. C* **92**, 044309 (2015).
- [47] A. Makinaga, R. Massarczyk, M. Beard, R. Schwengner, H. Otsu, T. Al-Abdullah, M. Anders, D. Bemmerer, R. Hannaske, R. John, A. R. Junghans, S. E. Müller, M. Röder, K. Schmidt, and A. Wagner, *Phys. Rev. C* **94**, 044304 (2016).
- [48] R. Schwengner, R. Massarczyk, K. Schmidt, K. Zuber, R. Beyer, D. Bemmerer, S. Hammer, A. Hartmann, T. Hensel, H. F. Hoffmann, A. R. Junghans, T. Kögler, S. E. Müller, M. Pichotta, S. Turkat, J. A. B. Turko, S. Uraß, and A. Wagner, *Phys. Rev. C* **105**, 024303 (2022).
- [49] G. Schramm, R. Massarczyk, A. R. Junghans, T. Belgya, R. Beyer, E. Birgersson, E. Grosse, M. Kempe, Z. Kis, K. Kosev, M. Krtička, A. Matic, K. D. Schilling, R. Schwengner, L. Szentmiklósi, A. Wagner, and J. L. Weil, *Phys. Rev. C* **85**, 014311 (2012).
- [50] R. Massarczyk, R. Schwengner, F. Dönau, E. Litvinova, G. Rusev, R. Beyer, R. Hannaske, A. R. Junghans, M. Kempe, J. H. Kelley, T. Kögler, K. Kosev, E. Kwan, M. Marta, A. Matic, C. Nair, R. Raut, K. D. Schilling, G. Schramm, D. Stach *et al.*, *Phys. Rev. C* **86**, 014319 (2012).
- [51] F. Bečvář, *Nucl. Instrum. Methods A* **417**, 434 (1998).
- [52] A. Gilbert and A. G. W. Cameron, *Can. J. Phys.* **43**, 1446 (1965).
- [53] T. von Egidy and D. Bucurescu, *Phys. Rev. C* **80**, 054310 (2009).
- [54] S. I. Al-Quraishi, S. M. Grimes, T. N. Massey, and D. A. Resler, *Phys. Rev. C* **67**, 015803 (2003).
- [55] C. E. Porter and R. G. Thomas, *Phys. Rev.* **104**, 483 (1956).
- [56] A. R. Junghans, G. Rusev, R. Schwengner, A. Wagner, and E. Grosse, *Phys. Lett. B* **670**, 200 (2008).
- [57] E. Grosse, A. R. Junghans, and R. Massarczyk, *Eur. Phys. J. A* **53**, 225 (2017).
- [58] S. Raman, C. W. Nestor, Jr., and P. Tikkanen, *At. Data Nucl. Data Tables* **78**, 1 (2001).
- [59] J.-P. Delaroche, M. Girod, J. Libert, H. Goutte, S. Hilaire, S. Péru, N. Pillet, and G. F. Bertsch, *Phys. Rev. C* **81**, 014303 (2010).
- [60] R. Capote, M. Herman, P. Obložinsky, P. G. Young, S. Goriely, T. Belgya, A. V. Ignatyuk, A. J. Koning, S. Hilaire, V. A. Plujko, M. Avrigeanu, O. Bersillon, M. B. Chadwick, T. Fukahori, Z. Ge, Y. Han, S. Kailas, J. Kopecky, V. M. Maslov, G. Reffo *et al.*, *Nucl. Data Sheets* **110**, 3107 (2009).
- [61] G. Rusev, R. Schwengner, R. Beyer, M. Erhard, E. Grosse, A. R. Junghans, K. Kosev, C. Nair, K. D. Schilling, A. Wagner, F. Dönau, and S. Frauendorf, *Phys. Rev. C* **79**, 061302(R) (2009).
- [62] R. Massarczyk, R. Schwengner, F. Dönau, S. Frauendorf, M. Anders, D. Bemmerer, R. Beyer, C. Bhatia, E. Birgersson, M. Butterling, Z. Elekes, A. Ferrari, M. E. Gooden, R. Hannaske, A. R. Junghans, M. Kempe, J. H. Kelley, T. Kögler, A. Matic, M. L. Menzel *et al.*, *Phys. Rev. Lett.* **112**, 072501 (2014).
- [63] A. Makinaga, R. Massarczyk, R. Schwengner, M. Beard, F. Dönau, M. Anders, D. Bemmerer, R. Beyer, R. Hannaske, A. R. Junghans, M. Kempe, T. Kögler, M. Röder, K. Schmidt, and A. Wagner, *Phys. Rev. C* **90**, 044301 (2014).
- [64] R. Massarczyk, G. Schramm, A. R. Junghans, R. Schwengner, M. Anders, T. Belgya, R. Beyer, E. Birgersson, A. Ferrari, E. Grosse, R. Hannaske, Z. Kis, T. Kögler, K. Kosev, M. Marta, L. Szentmiklósi, A. Wagner, and J. L. Weil, *Phys. Rev. C* **87**, 044306 (2013).
- [65] R. Massarczyk, G. Schramm, T. Belgya, R. Schwengner, R. Beyer, D. Bemmerer, Z. Elekes, E. Grosse, R. Hannaske, A. R. Junghans, Z. Kis, T. Kögler, C. Lorenz, K. Schmidt, L. Szentmiklósi, A. Wagner, and J. L. Weil, *Phys. Rev. C* **93**, 014301 (2016).
- [66] R. Massarczyk, G. Rusev, R. Schwengner, F. Dönau, C. Bhatia, M. E. Gooden, J. H. Kelley, A. P. Tonchev, and W. Tornow, *Phys. Rev. C* **90**, 054310 (2014).
- [67] A. V. Voinov, T. Renstrøm, D. L. Bleuel, S. M. Grimes, M. Guttormsen, A. C. Larsen, S. N. Liddick, G. Perdikakis, A. Spyrou, S. Akhtar, N. Alanazi, K. Brandenburg, C. R. Brune, T. W. Danley, S. Dhakal, P. Gastis, R. Giri, T. N. Massey, Z. Meisel, S. Nikas *et al.*, *Phys. Rev. C* **99**, 054609 (2019).
- [68] V. G. Soloviev, *Theory of Complex Nuclei* (Pergamon Press, Oxford, 1976).
- [69] V. Yu. Ponomarev, Ch. Stoyanov, N. Tsoneva, and M. Grinberg, *Nucl. Phys. A* **635**, 470 (1998).
- [70] M. Grinberg and Ch. Stoyanov, *Nucl. Phys. A* **573**, 231 (1994).
- [71] M. Spieker, A. Heusler, B. A. Brown, T. Faestermann, R. Hertenberger, G. Potel, M. Scheck, N. Tsoneva, M. Weinert, H.-F. Wirth, and A. Zilges, *Phys. Rev. Lett.* **125**, 102503 (2020).
- [72] M. Weinert, M. Spieker, G. Potel, N. Tsoneva, M. Müscher, J. Wilhelmy, and A. Zilges, *Phys. Rev. Lett.* **127**, 242501 (2021).
- [73] V. G. Soloviev, *Theory of Atomic Nuclei: Quasiparticles and Phonons* (Institute of Physics Publications, Bristol, UK, 1992).